PAPER

Magnetic relaxation switching assay based on three-dimensional assembly of Fe₃O₄@ZIF-8 for detection of cadmium ions†

Zhou Xu, [iD] [a] ShiQin Dai,[a] YiXuan Wang,[a] YanQiu Chen,[a] Yun-Hui Cheng[ac] and Shuang Peng*[ab]

The design and construction of a novel magnetic resonance switch (MRS) sensor for cadmium ion (Cd^{2+}) detection is described. Fe₃O₄@ZIF-8 was synthesized through seed-mediated growth of dimercaptosuccinic acid-coated Fe₃O₄. Fe₃O₄@ZIF-8 with high relaxation value (163.086 mM^{-1} s^{-1}) and large negative zeta potential (−20.69 mV) exhibited good magnetic relaxation performance and water solubility. The successfully synthesized Fe₃O₄@ZIF-8 was used to develop an immune recognition-based MOFs-MRS sensor for highly sensitive detection of Cd^{2+}. The proposed MRS detected a wide linear range of Cd^{2+} concentration from 2 to 200 ng mL^{-1} with a low limit of detection of 0.65 ng mL^{-1} (S/N = 3), and displayed high selectivity towards matrix interference. The robust sensing system was effective even in a complex sample matrix, enabling the quantitative analysis of Cd^{2+} content in rice samples and drinking water samples with good reliability. Recoveries of Cd^{2+} ranged from 91.50 to 112.05% for spiked drinking water and from 95.86 to 110.45% for spiked rice samples. The versatility of Fe₃O₄@ZIF-8 with customized relaxation responses could allow the adaptation of magnetic resonance platforms for food safety purposes.

Introduction

Heavy metal pollutants have attracted increasing public attention in recent years due to their serious threat to human health and the environment.[1–5] Highly sensitive and accurate detection of heavy metal contamination in food and environmental samples is important for public health. Cadmium ions (Cd^{2+}) are a typical heavy metal contaminant. Excess Cd^{2+} seriously threatens human health and can lead to serious diseases, including diarrhea, stomach pains, severe vomiting, bone fracture, reproductive failure and possibly even infertility, damage to the central nervous system and immune system, psychological disorders, and possibly DNA damage.[6–8] The World Health Organization has mandated that the concentration of Cd^{2+} in drinking water and air should be <0.005 mg L^{-1} and <5 ng m^{-3}, respectively.[9] Traditional Cd^{2+} detection methods include inductively coupled plasma-mass spectrometry (ICP-MS)[10] and atomic absorption/fluorescence

[a]*Hunan Provincial Key Laboratory of Cytochemistry, School of Food Science and Bioengineering, Changsha University of Science & Technology, Changsha 410114, P. R. China. E-mail: Ps20220414@163.com*

[b]*College of Chemistry and Chemical Engineering, Hunan University, Changsha, 410082, Hunan, China*

[c]*School of Food Science and Engineering, Qilu University of Technology, Jinan, Shandong, 250353, China*

† Electronic supplementary information (ESI) available. See https://doi.org/10.1039/d2ra03926e

spectrometry.[11,12] These methods have high detection sensitivity and reliable detection. However, requirements for complex sample pretreatment, skilled technicians, and expensive instruments have limited their widespread application in routine testing. Therefore, it to design fast, low-cost, and reliable detection methods for Cd^{2+} analysis in real samples.

The boom in nanotechnology is driving the development of traditional analytical methods. A variety of sensors have been developed to sensing metal pollutants. These include optical sensors and electrochemical sensors.[13,14] However, considering their susceptibility to interferences from the impurities, optical and electrochemical detections usually demand complicated sample pretreatments. In contrast, the magnetic relaxation switching (MRS) biosensor can be utilized in turbid and light-impermeable media without separation and purification steps.[15–17] It has been widely used to analyze different targets, including heavy metals,[18] DNA,[19] viruses,[20] bacteria,[21] pesticide residues,[22,23] hormones,[24] and antibiotics.[25,26] The principles of conventional MRS biosensors generally rely on dispersion/aggregation or altered concentration of magnetic nanoparticles (MNPs).[27,28] The unstable dispersion/aggregation and broad-size distribution of traditional MNPs compromises the sensitivity of MRS sensors.[29] To address these issues, the synthesis of highly disperse magnetic materials with high relaxation rates magnetic materials could more effectively modulate the relaxation behavior of water molecules, thus increasing the sensitivity of MRS biosensors.

Metal–organic frameworks (MOFs), an important kind of porous inorganic–organic hybrid materials with inherent outstanding physicochemistry characteristics, can be widely applied for the facile preparation of MOFs magnetic nanoporous materials.[30–32] The porous structure and high specific surface area of MOFs magnetic nanoporous materials can effectively host significant amounts of MNPs, which prevents their aggregation.[33] In addition, the porous structures and high specific surface areas of MOFs magnetic nanoporous materials impeded the access of water molecules into the MNP particle core. It reduced the self-diffusion coefficient of the vicinity water molecules, which increased the r_2 value (r_2, the indicator of magnetic relaxation performances). The high r_2 value and exceptional chemical stability will help improve the performance of detecting MRS sensors.[34,35] However, reports of MRS biosensors based on MOFs materials have been very limited in the literature. Based on our previous findings, MOFs magnetic nanoporous materials (Fe$_3$O$_4$@NPC) are excellent signal labels for enhanced magnetic relaxation switch signals that can be applied to MRS sensors.[36] But, the poorly dispersed and low r_2 value of these magnetic nanoporous materials problems for the MRS sensor detection performance. Therefore, synthesizing novel MOFs magnetic nanoporous materials with higher magnetic relaxation performances is crucial for improving the performance of MRS sensors.

In this work, we reported the Fe$_3$O$_4$@zeolite imidazolate framework-8 (ZIF-8) composites obtained through seed-mediated growth of dimercaptosuccinic acid (DMSA)-coated Fe$_3$O$_4$. It was exciting to find that the Fe$_3$O$_4$@ZIF-8 with higher relaxation values and large negative zeta potentials exhibited excellent magnetic relaxation performances and good water solubility. Based on the Fe$_3$O$_4$@ZIF-8, we developed an immune recognition-based MOFs-MRS sensor for highly sensitive detection of Cd^{2+} (Scheme 1). The detection mechanism is based on the change in T_2 relaxation time caused by the assembly and disassembly of Fe$_3$O$_4$@ZIF-8 through immune recognition. In the absence of Cd^{2+}, antibody (Ab)-Fe$_3$O$_4$@ZIF-8 and antigen (Ag)-Fe$_3$O$_4$@ZIF-8 assembled by immunological recognition, which makes a low change in the T_2 value. However, in the presence of Cd^{2+} strongly recognize with Ab-Fe$_3$O$_4$@ZIF-8 prevented the assembly of Ab-Fe$_3$O$_4$@ZIF-8 with
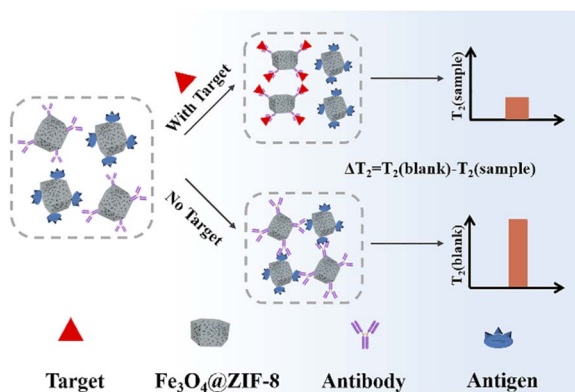
Ag-Fe$_3$O$_4$@ZIF-8, which decreased the T_2 value and increased ΔT_2 (denoted as the change of the T_2 value). Experimental results validated that the MOFs-MRS exhibited good sensitivity and a low detection limit (LOD) to determine Cd^{2+} in practical applications.

Results and discussion

Preparation and characterization of Fe$_3$O$_4$@ZIF-8

We prepared and characterized Fe$_3$O$_4$@ZIF-8 for the MRS sensor. The Fe$_3$O$_4$ was modified by DMSA (Fe$_3$O$_4$-DMSA), a small molecule with multiple carboxyl and mercapto functional groups. Fe$_3$O$_4$@ZIF-8 was obtained through seed-mediated growth of Fe$_3$O$_4$-DMSA. Transmission electron microscopy (TEM) was used to characterize the morphology of Fe$_3$O$_4$-DMSA and Fe$_3$O$_4$@ZIF-8. As shown in Fig. S1,† ZIF-8 exhibit the rhombic shape and have an average diameter of 179 nm. The morphology of Fe$_3$O$_4$@ZIF-8 composite is not markedly altered but the particle size is smaller (174 nm, Fig. 1C), because of the presence of heterogeneous nucleation process that typically leads to smaller crystals.[37,38]

To further confirm the synthesis of Fe$_3$O$_4$@ZIF-8, we performed Fourier transform infrared spectroscopy (FTIR), X-ray diffraction (XRD) and X-ray Photoelectron spectroscopy (XPS) for Fe$_3$O$_4$-DMSA, ZIF-8, and Fe$_3$O$_4$@ZIF-8. The Fe$_3$O$_4$-DMSA has the characteristic peak of Fe–O vibration band in 615 cm^{-1}, and the ZIF-8 has characteristic peaks in 759, 1150, and 1583 cm^{-1}. Three peaks at 759 cm^{-1}, 1150 cm^{-1} and 1583 cm^{-1} were observed in the spectrum of Fe$_3$O$_4$@ZIF-8, which reflected the existence of Fe$_3$O$_4$ nanoparticles.[39] The XRD peaks for Fe$_3$O$_4$@ZIF-8 are in line with the peaks of ZIF-8 at low angles of 5–20° and that of Fe$_3$O$_4$-DMSA at angles of 30°, 35°, 57°, and 63°, indicating the formation of Fe$_3$O$_4$@ZIF-8 composites. As shown in Fig. S3(A),† the XPS spectra of Fe$_3$O$_4$@ZIF-8 indicated the

Scheme 1 Principle of immune recognition-based MOFs-MRS sensor.

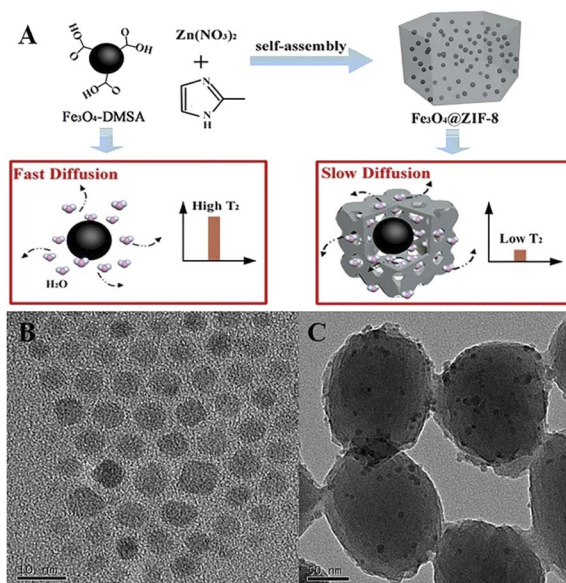Fig. 1 (A) Synthesis process of Fe$_3$O$_4$@ZIF-8. (B and C) TEM images of the Fe$_3$O$_4$-DMSA (B) and Fe$_3$O$_4$@ZIF-8 (C).

presence of carbon, nitrogen, oxygen, iron, and zinc species.[40] The Zn 2p spectra of Fe₃O₄@ZIF-8 showed that the spin orbitals of Zn 2p$_{1/2}$ and Zn 2p$_{3/2}$ have strong signals at 1045.00 eV and 1022.00 eV, respectively, demonstrating the existence of divalent Zn in the as-synthesized corresponding to characteristic peaks of ZIF-8. One peak at 615 cm^{-1} Fe₃O₄@ZIF-8. The C 1s spectrum showed that C-sp³, C–O and C=O groups are corresponding at 284.82 eV, 285.83 eV and 288.62 eV, respectively.[41] Displayed that the O 1s spectra consisting of three components with binding energies at 532.1, 331.57 eV and 531.28 eV, which were associated with C–OH, C–O, and Fe–O.[42] We also measured the concentration of Fe by Inductive Coupled Plasma Emission Spectrometer (ICP), the Fe concentration of ZIF-8 and Fe₃O₄@ZIF-8 were 0.01% and 4.29%, which significant indicated Fe₃O₄-DMSA exists in the Fe₃O₄@ZIF-8. These characterized and confirmed the preparation of the nanocomposite we designed.

Additionally, the N₂ sorption isotherms were also examined to analyze the porous structure of the Fe₃O₄@ZIF-8.[43] The nitrogen adsorption/desorption curves of the Fe₃O₄@ZIF-8 were type III curves with a relative pressure in the range of 0.8 to 1.0 with a significant hysteresis loop (Fig. 2C), suggesting a micro/mesoporous structure characteristic of Fe₃O₄@ZIF-8. The average Barrett–Joyner–Halenda (BJH) adsorption pore sizes of the Fe₃O₄@ZIF-8 was 1.76 nm (Fig. 2C). These results indicated that micro-mesopores contributed significantly to the pore volumes of the Fe₃O₄@ZIF-8 nanostructures. The proton transverse relaxation performance of materials is essential for the successful construction of an MRS sensor.[17] Fig. 2D and E show that the transverse relaxation rate (r_2, the indicators of magnetic relaxation performances) of Fe₃O₄@ZIF-8 (163.086
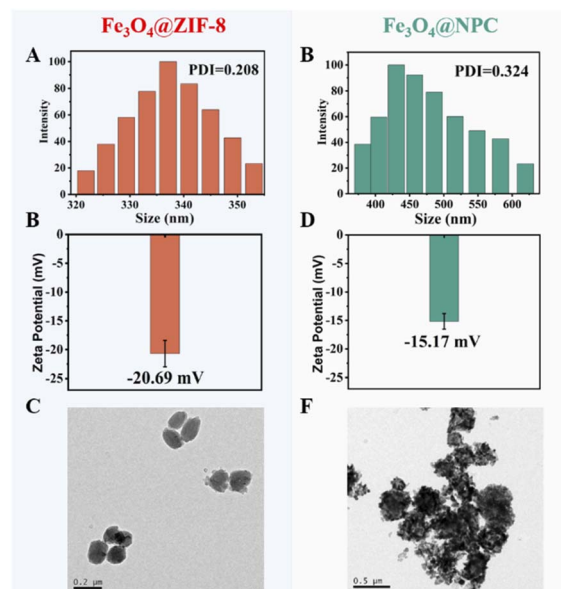

Fig. 3 (A and B) Size distribution of Fe₃O₄@ZIF-8 (A) and Fe₃O₄@NPC (B). (C and D) Zeta potential of Fe₃O₄@ZIF-8 (C) and Fe₃O₄@NPC (D). (E and F) TEM image of Fe₃O₄@ZIF-8 (E) and Fe₃O₄@NPC (F).

mM^{-1} s^{-1}) was higher than Fe₃O₄-DMSA (34.164 mM^{-1} s^{-1}). In addition, the Fe₃O₄@ZIF-8 displayed a higher r_2 value than Fe₃O₄@NPC (163.086 vs. 112.676 mM^{-1} s^{-1}). The apparent increase in the r_2 value will help improve the performance of Fe₃O₄@ZIF-8 in MRS sensor.

Dynamic light scattering (DLS), transmission electron microscopy (TEM), and electrophoretic light scattering (ELS)
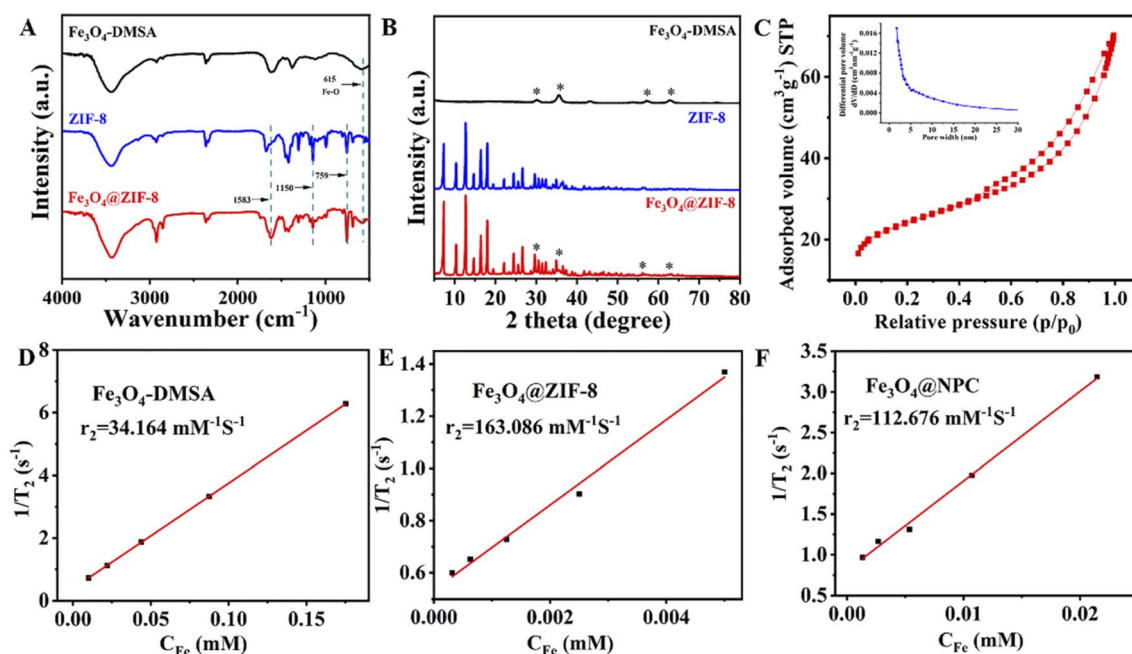

Fig. 2 (A) FTIR spectroscopy of Fe₃O₄-DMSA, ZIF-8, and Fe₃O₄@ZIF-8. (B) XRD patterns of Fe₃O₄-DMSA, ZIF-8, and Fe₃O₄@ZIF-8. (C) N₂ absorption–desorption isotherms and pore distributions of Fe₃O₄@ZIF-8. (D–F) Transverse relaxation rate of Fe₃O₄-DMSA (D) Fe₃O₄@ZIF-8 (E), and Fe₃O₄@NPC (F).

were used to characterize the dispersity of Fe_3O_4@ZIF-8. As shown in Fig. 3A the hydrated particle diameter of Fe_3O_4@ZIF-8 was 337 nm. The average hydro-diameter of Fe_3O_4@ZIF-8 were larger than the actual diameters of that, which were similar to previous reports.[44,45]

The particle polymer dispersity index (PDI) of Fe_3O_4@ZIF-8 (0.208) was lower than that of Fe_3O_4@NPC (0.324) (Fig. 3B). The zeta potential of Fe_3O_4@ZIF-8 of -20.69 mV (Fig. 3C) was lower than that of Fe_3O_4@NPC (-15.8 mV) (Fig. 3D). Negative zeta potentials can effectively inhibit aggregation of nanoparticles due to electric repulsion.[46,47] TEM revealed a greater dispersity of Fe_3O_4@ZIF-8 compared to Fe_3O_4@NPC (Fig. 3E and F). The collective results demonstrated the good dispersion of Fe_3O_4@ZIF-8, which is advantageous in constructing a sensitive MRS sensor. These results indicated that the Fe_3O_4@ZIF-8 exhibited good magnetic relaxation and water solubility, which will help improve the performance of the MOFs-MRS sensor.

Construction of Fe_3O_4@ZIF-8-based MRS sensor

To illustrate the assembly of Ag-Fe_3O_4@ZIF-8 and Ab-Fe_3O_4@-ZIF-8, we evaluated the hydration particle size and zeta potentials using DLS and ELS. Fe_3O_4@ZIF-8 were coated with Cd^{2+}-specific antibodies and Cd^{2+}-specific antigens to form Ab-Fe_3O_4@ZIF-8 and Ag-Fe_3O_4@ZIF-8, respectively. The hydration particle size of Ab-Fe_3O_4@ZIF-8 increased from 337 nm to 398 nm and that of Ag-Fe_3O_4@ZIF-8 from 337 nm to 390 nm (Fig. 4B). Their zeta potentials decreased from -20.69 mV to -28.69 mV and -28.72 mV, respectively (Fig. 4A). After the biological immune recognition, the hydration particle size of assembly objects changed obviously (910.27 nm) (Fig. 4B). These results indicated that the antibody and antigen successfully modify the surface of Fe_3O_4@ZIF-8. To evaluate the feasibility of the Ag-Fe_3O_4@ZIF-8 and Ab-Fe_3O_4@ZIF-8 assembly in the construction of the MRS sensor, we measured the T_2

relaxation time of Ag-Fe_3O_4@ZIF-8, Ab-Fe_3O_4@ZIF-8, and assembly. As shown in Fig. 4C, the T_2 relaxation time of the assembly (881.864 ms) was higher than that of Ab-Fe_3O_4@ZIF-8 (689.104 ms) and Ag-Fe_3O_4@ZIF-8 (731.368 ms). The findings indicated that assembly increased the transverse relaxation time and confirmed the feasibility of Fe_3O_4@ZIF-8 to construct the MRS immunosensor.

Optimization of detection conditions

To improve the analytical performance of the MRS, we optimized the concentration of Fe_3O_4@ZIF-8, antibodies/antigens, incubation time, and TE values. The ΔT_2 value increased with increasing Fe_3O_4@ZIF-8 concentration, and then maintained a decreasing amplitude after reaching 0.15 mg mL^{-1} (Fig. 5A). In this case, 0.15 mg mL^{-1} was selected for further investigation. The influence of the concentration of antibodies/antigens on changes in T_2 are shown in Fig. 5B. An antibody/antigen concentration of 4 µg mL^{-1} was the optimum concentration. Fig. 5C shows the optimized reaction times; ΔT_2 increased gradually with increasing reaction time from 20 min to 100 min. Subsequently, ΔT_2 reached a plateau after 60 min, indicating that the Cd^{2+}-induced assembly of NPs was fully achieved. Therefore, 60 min was used as the optimal reaction time for the following BPA detection. As shown in Fig. 5D, the maximum value of ΔT_2 was observed at a TE of 2 ms, which was selected for the subsequent experiments. To ensure accurate results, the optimal conditions were used in subsequent detections.

Detection of Cd^{2+} by MRS sensor

We employed the Ag-Fe_3O_4@ZIF-8 and Ab-Fe_3O_4@ZIF-8 to construct a MOFs-MRS sensor for the detection of Cd^{2+}. The detection mechanism is based on the change in T_2 relaxation time caused by the assembly and disassembly of Fe_3O_4@ZIF-8 through immune recognition. In the absence of Cd^{2+}, Ab-Fe_3O_4@ZIF-8 with Ag-Fe_3O_4@ZIF-8 leads to an immunological recognition-based assembly, which makes a low change in the
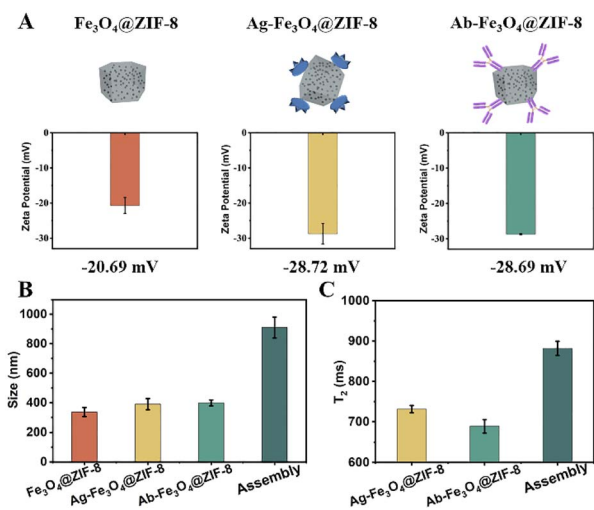

Fig. 4 (A) Zeta potential of Fe_3O_4@ZIF-8, Ag-Fe_3O_4@ZIF-8, and Ab-Fe_3O_4@ZIF-8. (B) Hydrated particle size of Fe_3O_4@ZIF-8, Ag-Fe_3O_4@ZIF-8, Ab-Fe_3O_4@ZIF-8, and Assembly. (C) T_2 relaxation time of Ag-Fe_3O_4@ZIF-8, Ab-Fe_3O_4@ZIF-8, and Assembly.
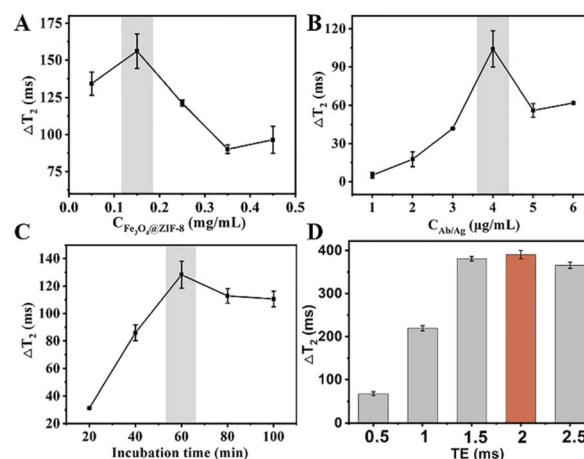

Fig. 5 Condition optimization of the MRS biosensor. (A–D) Effect of the Fe_3O_4@ZIF-8 concentration (A), antigen/antibody concentration (B), incubation time (C), and echo time (D).
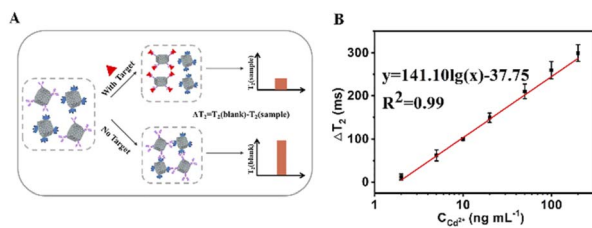
Fig. 6 (A) Scheme of immune recognition-based MRS sensor for highly sensitive detection of the Cd^{2+}. (B) Standard curve for detecting Cd^{2+}. The concentrations of Cd^{2+} ranged from 2 to 200 ng mL^{-1}. Error bars represent the standard deviation of three replicates ($n = 3$).

T_2 value. In contrast, exposure of Cd^{2+} to the system will break the assembly process (disassembly) based on the competition effect of Cd^{2+} with Cd^{2+}-Ag to strongly recognize Ab-Fe_3O_4@ZIF-8. This decreases the T_2 value and increases ΔT_2 (denoted as the change of the T_2 value) (Fig. 6A). The assembly degree of Fe_3O_4@ZIF-8 is related to the concentration of Cd^{2+}. Under optimized conditions, a linear relationship was obtained between ΔT_2 and the concentration of Cd^{2+} from 2 to 200 ng mL^{-1}. The linear equation was $y = 141.10\lg(x) - 37.75$ ($R^2 = 0.99$). The limit of detection (LOD) was 0.65 ng mL^{-1}, calculated by $3\sigma b$/slope (σb, standard deviation of the blank samples). The LOD was lower than that of the other MRS and other conventional sensitive detection methods (Table S1†).

Specificity analysis

To assess the selectivity of the MRS platform for Cd^{2+} detection, several metal ions, including K^+, Na^+, Fe^{2+}, Mg^{2+}, Ca^{2+}, Pd^{2+},

Ba^{2+}, Zn^{2+}, and Ag^+, were tested in the same way. As shown in Fig. 7, Cd^{2+} resulted in a remarkable value of ΔT_2. Other metal ions failed to generate obvious ΔT_2 value in the sensing system. The data demonstrated that this sensing platform possessed excellent specificity for the Cd^{2+} assay. The control heavy metal ions did not disturb the biosensor response. This high specificity can be ascribed to the high binding capability between Cd^{2+} and antibody.

Real sample analysis

To demonstrate the practical applications of the sensing platform, this biosensor was applied to the detection of Cd^{2+} in drinking water and rice samples. The results as depicted in Table 1. The measured Cd^{2+} in rice samples agree well with the added concentrations with the recoveries of 91.50% to 112.05% and a relative standard deviation (RSD) of 1.05% to 11.74%. Also, the measured Cd^{2+} in drinking water agreed well with the added concentrations with the recoveries of 95.85% to 110.44% as well as relative RSD of 2.14% to 9.69%.[48] The findings revealed that the magnetic sensor can be applied in the practical sample detection, with good accuracy and sensitivity for Cd^{2+} detection in food samples.

Conclusions

In conclusion, we generated Fe_3O_4@ZIF-8 with high relaxation values and excellent dispersion. Based on the Fe_3O_4@ZIF-8, we establish a versatile immune recognition-based MOFs-MRS sensing system for sensitive detection of the Cd^{2+} in the real sample. The optimized MOFs-MRS displayed a broad quantitative range from 2 to 200 ng mL^{-1} and a limit of detection 0.65 ng mL^{-1}. When tested using samples of rice and drinking water, the MOFs-MRS was conferred with a satisfactory recovery (91.50% to 112.05%). The findings also detail the improved dispersion and relaxation values of MOFs magnetic nanoporous materials, and are a novel approach to improve the performance of MOFs-based MRS sensor. Moreover, the MOFs-MRS sensing system could be expected to detect other food hazard factors by simply replacing antibody/antigen.

Experimental

Preparation of Fe_3O_4@ZIF-8

Fe_3O_4-DMSA was synthesized following as previously described with slight modifications.[35] Then, 0.003 mol of zinc nitrate
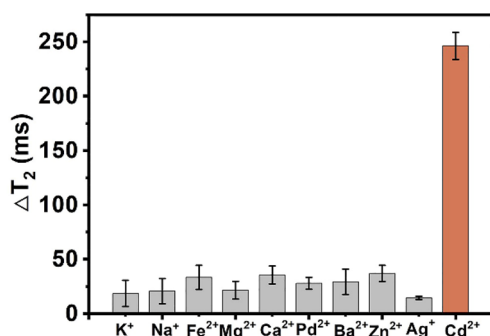

Fig. 7 Selectivity testing of the sensing system for Cd^{2+} and some control metal ions. Error bars represent the standard deviation of three replicates ($n = 3$).

Table 1 Analytical parameters of the proposed method for determining Cd^{2+} drinking water and rice samples

Sample	Added concentration (ng mL^{-1})	Detected concentration (ng mL^{-1})	RSD ($n = 3$, %)	Recovery ($n = 3$, %)
Rice	50	45.75 ± 0.48	1.05	91.50 ± 0.96
	20	22.41 ± 2.63	11.74	112.05 ± 13.15
	2	1.99 ± 0.03	1.50	99.50 ± 1.50
Drinking water	50	55.22 ± 3.97	7.19	110.44 ± 7.94
	20	19.17 ± 1.86	9.70	95.85 ± 9.30
	2	1.96 ± 0.04	2.04	98.00 ± 2.00

hexahydrate was dissolved in 100 mL of N, N-Dimethylformamide (DMF, liquid A), and 0.006 mol of 2-methylimidazole was dissolved in 100 mL of DMF (liquid B). 1 mL of zinc nitrate hexahydrate and 9 mL of Fe_3O_4-DMSA (1.5 mg mL^{-1}) solution were mixed in a 50 mL conical flask as the starting solution and heated in a water bath at 40 °C. 10 mL of both liquid A and liquid B were added to 10 mL of the initial solution using a syringe pump at a flow rate of 20 mL h^{-1} at a constant speed. After 30 min of reaction, 20 mL of the solution was collected from the reaction system. This represented the first growth product. 10 mL of the first growth product were used as the starting solution. 10 mL of both liquid A and liquid B were injected using a syringe pump at a flow rate of 20 mL h^{-1} at a constant speed. The second growth product was obtained by reaction for 1 h. For pure ZIF-8, the Fe_3O_4-DMSA is omitted and substituted with an equivalent amount of DI water.

Preparation of functional Fe_3O_4@ZIF-8

We used the covalent coupling method to immobilize the antibodies/antigens on the Fe_3O_4@ZIF-8 surfaces. Antigen-Fe_3O_4@ZIF-8 (Ag-Fe_3O_4@ZIF-8) was prepared by adding 1 mL Fe_3O_4@ZIF-8, 2 mL of 4 µg mL^{-1} antigen solution, 0.5 mL of 10 mg mL^{-1} EDC solution, 0.2 mL of 10 mg mL^{-1} sulfo-NHS solution, and 2 mL of 0.5 mg mL^{-1} Fe_3O_4@ZIF-8 solution to a 10 mL centrifuge tube. The mixture was reacted at room temperature for 12 h to allow the coupling. Excess antibody was removed by centrifugation. Preparation of Ab-Fe_3O_4@ZIF-8 was similar to that of Ag-Fe_3O_4@ZIF-8 by simply replacing antigen with antibody.

Optimization of relaxation sensing system conditions

Concentrations of Fe_3O_4@ZIF-8 were optimized at 0.05, 0.15, 0.25, 0.35 and 0.45 mg mL^{-1} according to the ΔT_2 value. At the same concentration of Fe_3O_4@ZIF-8 (0.15 mg mL^{-1}), antibody/antigen concentrations were optimized as 2, 4, 6, 8, and 10 µg mL^{-1}. The incubation time was optimized as 20, 40, 60, 80, 100, and 120 min (0.15 mg mL^{-1} Fe_3O_4@ZIF-8, 4 µg mL^{-1} antibody/antigen). Finally, we selected the echo time (TE) of test parameters as 0.5, 1, 1.5, 2, and 2.5 ms.

Detection of Cd^{2+}

Establishment of Cd^{2+} standard curve. 150 µL of Ab-Fe_3O_4@ZIF-8 (0.15 mg mL^{-1}) and Ag-Fe_3O_4@ZIF-8 (0.15 mg mL^{-1}) were mixed with different concentrations of Cd^{2+} (2, 5, 10, 20, 50, 100, and 200 ng mL^{-1}). The mixture was incubated at room temperature for 60 min. After 2 min of equilibrium, T_2 relaxation time was measured using NMI 20-CA at room temperature. The ΔT_2 was calculated as $\Delta T_2 = T_2(\text{Blank}) - T_2(\text{Sample})$, where the T_2(Blank) is the relaxation time of Fe_3O_4@ZIF-8 solution without Cd^{2+} and T_2(Sample) is the relaxation time of test solution with different concentrations of Cd^{2+}.

Detection of Cd^{2+} in real samples. In order to test the Cd^{2+} level in drinking water and rice samples, pretreatment of the samples was carried out: the rice was ground into rice flour, 0.4 g of rice flour was put into a tetrafluoroethylene tank and soaked overnight with 5 mL nitric acid. 2 mL hydrogen peroxide

solution (30%) of zinc nitrate hexahydrate was added in it, and keeping in the drying oven at 120 °C for 5 h. Then, the sample was heated to evaporate acid and make it close to dry. Pour the digestive liquid into a 25 mL volumetric flask, and use ultrapure water for constant volume. The pre-treatment of water samples is to obtain Ipoh water from the laboratory using a 10 mL centrifuge tube, centrifuge and remove the supernatant. We take 300 µL drinking water and rice digestion solution, and T_2 measurement was performed with 0.5 T nuclear magnetic resonance (NMR) instrument. At least three tests were performed. Next, food samples were adulterated with known levels of Cd^{2+} and tested for recovery. Three concentrations of Cd^{2+} were added to mineral water and rice digestion solution, and the final concentrations of Cd^{2+} were 2 ng mL^{-1}, 20 ng mL^{-1}, and 50 ng mL^{-1}. The measured mean values were then obtained using the following dose response equation of the sensor.

Conflicts of interest

There are no conflicts of interest to declare.

Acknowledgements

References

1 S. Rajendran, T. A. K. Priya, K. S. Khoo, T. K. A. Hoang, H. S. Ng, H. S. H. Munawaroh, C. Karaman, Y. Orooji and P. L. Show, *Chemosphere*, 2022, **287**, 132369.

2 M. Mao, T. Yan, J. Shen, J. Zhang and D. Zhang, *Environ. Sci. Technol.*, 2021, **55**, 3333–3340.

3 P. Y. Wang, L. Li, X. P. Pang, Y. Zhang, Y. Zhang, W. F. Dong and R. H. Yan, *RSC Adv.*, 2021, **11**, 12015–12021.

4 H. Esmaeili, S. M. Mousavi, S. A. Hashemi, W.-H. Chiang and S. Ahmadpour Abnavi, *Carbon Lett.*, 2021, **31**, 851–862.

5 S. A. Hashemi, S. Bahrani, S. M. Mousavi, F. Mojoudi, N. Omidifar, K. B. Lankarani, M. Arjmand and S. Ramakrishna, *Chem. Eng. J.*, 2022, **440**, 135896.

6 T. Frangos and W. Maret, *Nutrients*, 2020, **13**, 53.

7 Y. Huang, Y. Dai, M. Li, L. Guo, C. Cao, Y. Huang, R. Ma, S. Qiu, X. Su, K. Zhong, Y. Huang, H. Gao and Q. Bu, *Sci. Total Environ.*, 2021, **797**, 149043.

8 S. A. Hashemi, S. Bahrani, S. M. Mousavi, N. Omidifar, M. Arjmand, K. B. Lankarani and S. Ramakrishna, *Eur. Polym. J.*, 2022, **162**, 110926.

9 D. H. Zhou, W. Wu, Q. Li, J. F. Pan and J. H. Chen, *Anal. Methods*, 2019, **11**, 3546–3551.

10 Y. Tian, J. Cheng, X. Han, Y. Li, T. Yang, M.-L. Chen, J. Ma and J.-H. Wang, *J. Anal. At. Spectrom.*, 2022, **37**, 157–164.

11 R. Pavadai and P. Perumal, *New J. Chem.*, 2022, **46**, 3431–3447.

12 C. T. Shi, Z. Y. Huang, A. B. Wu, Y. X. Hu, N. C. Wang, Y. Zhang, W. M. Shu and W. C. Yu, *RSC Adv.*, 2021, **11**, 29632–29660.

13 T. Li, T. Yao, C. Zhang, G. Liu, Y. She, M. Jin, F. Jin, S. Wang, H. Shao and J. Wang, *RSC Adv.*, 2016, **6**, 66949–66956.

14 A. D. Cabral, T. B. Radu, E. D. de Araujo and P. T. Gunning, *RSC Chem. Biol.*, 2021, **2**, 815–829.

15 Y. P. Chen and M. X. Xie, *RSC Adv.*, 2015, **5**, 95401–95404.

16 J. M. Perez, L. Josephson, T. O'Loughlin, D. Hogemann and R. Weissleder, *Nat. Biotechnol.*, 2002, **20**, 816–820.

17 Y. Xianyu, Y. Dong, Z. Zhang, Z. Wang, W. Yu, Z. Wang and Y. Chen, *Biosens. Bioelectron.*, 2020, **155**, 112106.

18 W. Jiang, S. Yang, X. Sun, W. Lu, D. Jiang, L. Xu, H. Xu, B. Gao, M. Ma and F. Cao, *Anal. Methods*, 2018, **10**, 2494–2502.

19 R. N. Silva and P. Zhang, *Methods Mol. Biol.*, 2022, **2393**, 611–622.

20 S. H. Liao, H. S. Huang, J. H. Chen, Y. K. Su and Y. F. Tong, *RSC Adv.*, 2018, **8**, 4057–4062.

21 X. Qi, Z. Wang, R. Lu, J. Liu, Y. Li and Y. Chen, *Food Chem.*, 2021, **338**, 127837.

22 W. Zheng, L. Zeng and Y. Chen, *Anal. Chem.*, 2020, **92**, 2787–2793.

23 Y. Dong, W. Zheng, D. Chen, X. Li, J. Wang, Z. Wang and Y. Chen, *New J. Chem.*, 2019, **67**, 9942–9949.

24 L. Wu, Y. L. Xianyu, Z. L. Wang, Y. Z. Dong, X. B. Hu and Y. P. Chen, *Anal. Chem.*, 2019, **91**, 15555–15562.

25 Y. Chen, Y. Xianyu, M. Dong, J. Zhang, W. Zheng, Z. Qian and X. Jiang, *Anal. Chem.*, 2018, **90**, 6906–6912.

26 Y. Xianyu, Y. Dong, Z. Wang, Z. Xu, R. Huang and Y. Chen, *ACS Sens*, 2019, **4**, 1942–1949.

27 Y. Yang, Y. Zhang, J.-C. Shen, H. Yang, Z.-G. Zhou and S.-P. Yang, *Chin. Chem. Lett.*, 2016, **27**, 891–895.

28 Y. Liu, Z. Cai, L. Sheng, M. Ma and X. Wang, *J. Hazard. Mater.*, 2020, **388**, 121728.

29 C. Min, H. Shao, M. Liong, T.-J. Yoon, R. Weissleder and H. Lee, *ACS Nano*, 2012, **6**, 6821–6828.

30 N. A. Schejn, T. Mazet, V. Falk, L. Balan, L. Aranda, G. Medjahdi and R. Schneider, *Dalton Trans.*, 2015, **44**, 10136–10140.

31 G. Lee, S. Lee, S. Oh, D. Kim and M. Oh, *J. Am. Chem. Soc.*, 2020, **142**, 3042.

32 H. C. Zhou, J. R. Long and O. M. Yaghi, *Chem. Rev.*, 2012, **112**, 673–674.

33 M. Aghayi-Anaraki and V. Safarifard, *Eur. J. Inorg. Chem.*, 2020, **2020**, 1916–1937.

34 H. Lu, Y. Xu, R. Qiao, Z. Lu, P. Wang, X. Zhang, A. Chen, L. Zou and Z. Wang, *Nano Res.*, 2020, **13**, 2216–2225.

35 Z. Xu, Y. Chen, M. Chen, W. Chen and Y. Cheng, *J. Mater. Chem. C*, 2021, **9**, 11915–11923.

36 Z. Xu, R. Wang, Y. Chen, M. Chen, J. Zhang, Y. Cheng, J. Xu and W. Chen, *Mikrochim. Acta*, 2021, **188**, 90.

37 R. Ricco, P. Wied, B. Nidetzky, H. Amenitsch and P. Falcaro, *Chem. Commun.*, 2020, **56**, 5775–5778.

38 A. Schejn, T. Mazet, V. Falk, L. Balan, L. Aranda, G. Medjahdi and R. Schneider, *Dalton Trans.*, 2015, **44**, 10136–10140.

39 J. Lin, P. Xin, L. An, Y. Xu, C. Tao, Q. Tian, Z. Zhou, B. Hu and S. Yang, *Chem. Commun.*, 2019, **55**, 478–481.

40 C. Huang, X. Qiao, W. Sun, H. Chen, X. Chen, L. Zhang and T. Wang, *Anal. Chem.*, 2019, **91**, 2418–2424.

41 J. Du, X. Chen, K. Liu, D. Zhao and Y. Bai, *Sens. Actuators, B*, 2022, **360**, 131654.

42 Y. Qu, L. Qin, X. Liu and Y. Yang, *Sep. Purif. Technol.*, 2022, **294**, 121169.

43 K. S. Park, Z. Ni, A. P. Côté, J. Y. Choi, R. Huang, F. J. Uribe-Romo, H. K. Chae, M. O'Keeffe and O. M. Yaghi, *Proc. Natl. Acad. Sci. U. S. A.*, 2006, **103**, 10186–10191.

44 L. Xu, H. Yin, W. Ma, L. Wang, H. Kuang and C. Xu, *J. Phys. Chem. B*, 2013, **117**, 14367–14371.

45 S. T. Dibaba, R. Y. Wei, W. S. Xi, L. Zhao, L. Y. Shi, W. Ren, T. Mayr and L. N. Sun, *RSC Adv.*, 2018, **8**, 35706–35718.

46 Y. H. Zhang, M. M. Zhao, Z. X. Ning, S. J. Yu, N. Tang and F. B. Zhou, *J. Agric. Food Chem.*, 2018, **66**, 4208–4218.

47 H. Ohshima, A. Miyagishima, T. Kurita, Y. Makino, Y. Iwao, T. Sonobe and S. Itai, *Int. J. Pharm.*, 2009, **377**, 180–184.

48 S. A. Hashemi, S. M. Mousavi, S. Bahrani, S. Ramakrishna and S. H. Hashemi, *Anal. Bioanal. Chem.*, 2020, **412**, 5353–5365.